Quantitative description of morphological transitions in diffusion-limited growth of xenon crystals

H. M. Singer* and J. H. Bilgram†

Laboratorium für Festkörperphysik, Eidgenössische Technische Hochschule, CH-8093 Zürich, Switzerland

Changes of growth morphologies are induced by a perturbation of the temperature distribution in the surrounding of a growing xenon crystal. Apart from the dendritic morphology seaweed and doublon morphologies are found. We present a method which quantitatively describes growth morphologies by means of rotational, scale, and translational invariant transformations. Evolutions of growth morphologies are represented as paths in the morphology space. The presented method could be of some use for other fields of research where qualitative and quantitative information of different classes of images has to be identified.

I. INTRODUCTION

The formation of patterns is universal in nature. Patterns are found, for example, on sea shells, snow crystals, magnetic domains, and grain structures in rocks [1]. The growth of a stable phase at the expense of a metastable phase is a prototype for the formation of complex spatio-temporal patterns far from equilibrium, which evolve from homogenous starting conditions. The solidification of metals during the casting process, where crystals grow into a constitutionally supercooled melt, is technologically significant. The microstructures formed during this process influence the mechanical properties and the corrosion behavior of the final product.

Dendrites are an example of spatial patterns and have been studied carefully since long ago. General reviews on dendritic solidification can be found in [2–6]. Although the governing equations for thermal solidification have been known for a long time (Stefan problem—e.g., [7]), it was only in the last decade that the understanding of pattern formation in nonlinear systems has remarkably improved. By means of mathematical studies for two-dimensional systems Brener *et al.* [8–10] developed a morphology diagram of patterns found in diffusional growth. The crucial physical parameters, which determine the structure of the pattern, are the supercooling (controlling the growth velocity) and the anisotropy of the surface tension (leading to nonaxisymmetric growth). In their morphology diagram Brener *et al.* have established stability regions of dendrites and seaweed. Seaweed structures were predicted to be found at sufficiently low anisotropy of surface tension and high supercoolings, dendrites at sufficiently low supercoolings and high enough anisotropy of surface tension. Seaweed and doublon structures were found experimentally by Akamatsu *et al.* [11] for solidification of an organic alloy in quasi two dimensions. Doublons and seaweed were also discovered in three-dimensional (3D) free growth experiments by Stalder and Bilgram [12] and characterized by Singer [13].

Brener *et al.* suggested the characterization of growth morphologies [8] by two different criteria: on the one hand,

it is distinguished between dendritic and seaweed structures and, on the other hand, between compact and fractal growth. The dendritic morphology is characterized as a pattern with orientational order whereas patterns without obvious orientational order are called seaweed. Compact growth is defined as growth at a constant average density. Fractal structures are defined as patterns with self-similar or self-affine internal structure with a scaling range of at least one order of magnitude in length scales.

We argue that this discrimination between the morphologies is not sufficient to characterize structures in 3D experiments because doublons in two and three dimensions possess a well-defined axis of symmetry. Thus an orientational order can be attributed to these structures, which would then lead to a classification as "dendrite." It has been stated that doublons in two dimensions are the basic building blocks of seaweed [10]. For thermal free growth in 3D experiments we do not find the same behavior as has been predicted for 2D systems because the topological freedom of structures in three dimensions is different from the one in two dimensions. Based on the experimental observation of transitions between 3D doublons and 3D seaweed we argue that doublons and seaweed have to be treated as separate morphology classes.

From the experimental point of view it is difficult to distinguish between compact and fractal growth as no determinations of densities of doublons and seaweed are available up to now. The only morphology classification left, which could be applied in experiments, is the orientational order. To obtain quantitative measures independently of the observer a simple symmetry determination (which involves the manual determination of the axis of growth) was not the best scheme to apply; therefore, we have developed a more suitable classification scheme. In this paper a method is presented to characterize growth morphologies quantitatively and thus allows characterization of crystal morphologies as a function of growth conditions.

II. EXPERIMENT

In our experiments we use the rare gas xenon as a model substance for metals because (i) it forms a "simple liquid,"

---

*Electronic address: hsinger@solid.phys.ethz.ch
†Electronic address: bilgram@solid.phys.ethz.ch

70 031601-1

(ii) it has a low melting entropy to form rough solid-liquid interfaces, and (iii) it crystallizes in fcc structure. Furthermore, xenon is transparent and allows optical *in situ* observation of the growth process. As xenon crystallizes in the fcc structure we find fourfold symmetry axes for dendritic growth and four fins along the dendrite's main axis. The side branches develop at the ridges of these fins.

In our *in situ* experiments we investigate three-dimensional xenon crystals during free growth into their supercooled melt. The undercooling of the melt is in the range of $40 \text{ mK} \leqslant \Delta T \leqslant 220 \text{ mK}$ (corresponding to about $0.6 \times 10^{-3} \leqslant \Delta \leqslant 4 \times 10^{-3}$ in dimensionless units, with $\Delta = \Delta T/L/c_p$, where ΔT, c_p, and L are supercooling, specific heat of the liquid, and latent heat, respectively) below the triple point ($T_t = 161.3897$ K). The experimental setup consists of a high-precision cryostat to stabilize temperature better than $\pm 10^{-4}$ K as long as necessary. The cryostat is cooled with liquid nitrogen. An adjustable helium gas atmosphere between the liquid nitrogen and the thermostating liquid (isopentane) allows the heat flux to be regulated. Temperature is measured by means of temperature sensitive resistors (Pt-100). Heating is controlled by a commercial proportional-integral-differential (PID) controller. A stirrer in the thermostating liquid is producing a laminar flow and hence ensures a homogenous temperature in the heat bath. The actual growth vessel is immersed in the heat bath. In order to initiate the growth of the crystal we use the capillary injection technique [14]: A capillary reaches into the growth vessel, which is filled with liquid supercooled xenon. Upon initiation the crystal is growing along the capillary until it reaches the end and subsequently enters the state of free three-dimensional thermal growth. The experimental apparatus allows us to turn the capillary along its axis in order to orient the crystal so that the maximal projection area can be observed. It also allows us to shift the capillary up and down (vertical translation) in order to follow the crystal during its growth. A sketch of our experimental setup is given in Fig. 1.

A self-built optical imaging system (periscope) allows us to observe the crystal during its free growth. We have tested the optical resolution of the periscope to be 1.22 μm. We use a spatially homogenous cold light source to illuminate the crystal. Xenon is optically transparent in liquid and solid states. The crystal can therefore only be seen due to the difference of the indices of refraction ($n_{\text{liquid}} = 1.3918$, $n_{\text{solid}} = 1.4507$ for $\lambda = 546$ nm) [15,16]. By means of a beam splitter and two cameras the images of growing crystals are recorded simultaneously by a high-resolution digital charge-coupled-device (CCD) camera (1280×1024 pixels) on a computer and by an analog SVHS video with standard resolution (576×768 pixels, 25 frames per second). This double strategy was chosen in order to investigate different aspects of the growth. The images of the digital camera are used for detailed studies of the shape (geometrical aspects) whereas video sequences are used for characterizing the dynamics of the system (e.g., growth velocity). The image capture software was developed in our laboratory: the software is able to capture images at a speed of up to seven frames per second with the given hardware of the PCI board. Images can be taken manually or timer based. In our experiments a typical time interval between image capture is $1-5$ s. These images

are stored as 8-bit Tiff images and are analyzed after the experiment. A more detailed description of the experimental setup can be found in [13,17,18].

In Fig. 2 images of three morphologies 2(a) dendrites, 2(b) doublons, and 2(c) seaweed are given. Prototypically these different morphologies have following properties.

Dendrite. The dendritic morphology possesses a fourfold symmetry perpendicular to the axis of growth. On the four fins side branches start growing. Although no direct coupling between the fins exists the frequency of the side branch appearance is (prototypically) the same on each fin and crystals show a strong mirror symmetry. The tip of the dendrite up to a certain height does not show any side branches. Although it is a still ongoing dispute on the exact shape of the dendrite tip [19,20], it can be stated at least that its appearance is convex and usually spear like. In a moving frame of reference, where the dendrite tip is placed in the origin, the shape of the tip and the fins does not change. The side branches move upwards, grow longer and interact with their neighbors.

Doublon. The doublon morphology exhibits one symmetry plane. The prototypical characteristic of this morphology is that two main tips grow simultaneously and in parallel, influencing and stabilizing each other. The creation of a doublon starts with the splitting of the main tip of a dendrite. The two tips evolve with the same velocity and hinder each other to outgrow the other tip unless experimental inhomogeneities are perturbing the system. While doublons in two dimensions possess a protected channel this is obviously not the case in three dimensions. The 3D structure is topologically different from its two-dimensional pendant.

Seaweed. The seaweed morphology possesses neither any apparent symmetry nor a distinct main tip in the projection. The main property of this morphology is the continuous tip splitting for any prominent tip (also side branches) in its temporal evolution: the local tip radius increases until it reaches a critical value, which causes the structure to split ("tip splitting"). One of the two tips is immediately outgrowing the other one and starts increasing its tip radius again whereas the other decelerates its growth and eventually stops growing.

III. GROWING DIFFERENT MORPHOLOGIES

As mentioned in the previous section the growing crystal can be turned and translated in the growth vessel. Although every motion of the crystal in the melt is a perturbation of the thermal environment of the crystal, measurements of the tip radius have shown that "slow" changes (i.e., comparable to the growth velocity of the crystal) do not disturb the crystal in its growth. This allows us to observe the growth of crystals over distances, which are longer than the way to cross the field of vision of the periscope.

If a shift or a turn of the crystal is performed "fast," then the thermal environment of the growing crystal is changed significantly. By such a procedure it is possible to induce morphology changes of the crystals. The method found by Stalder and Bilgram [12] is as follows: The crystal is shifted downwards to regions in the growth vessel where the tem-
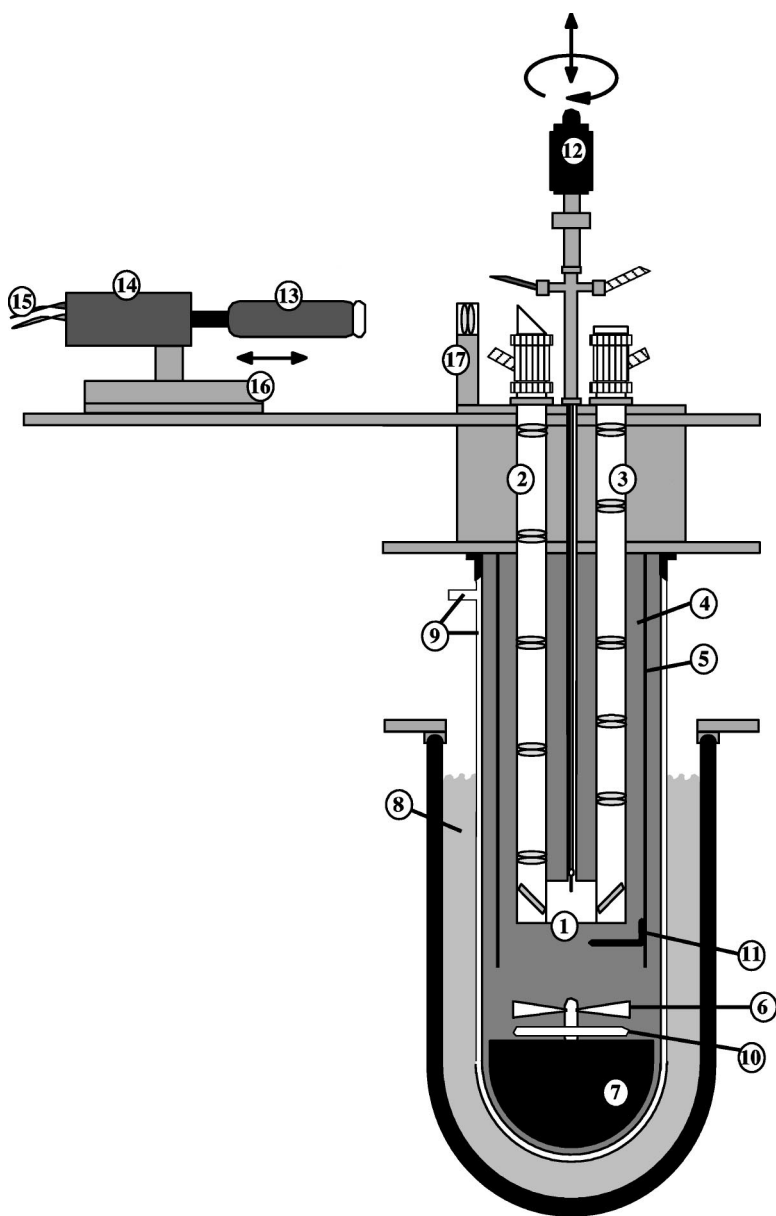
FIG. 1. Experimental setup: 1, growth vessel with the capillary; 2, periscope; 3, illumination system; 4, heat bath (isopentane); 5, tube to provide a laminar flow; 6, stirrer; 7, big mass of stainless steel to reduce the vibrations of the stirrer; 8, liquid nitrogen; 9, adjustable helium gas atmosphere to control the cooling power; 10, heater; 11, temperature sensor; 12, combined rotary and linear motion drive to lift and to rotate the capillary; 13, zoom lens ($1\times$-$7\times$); 14, digital CCD-camera and analog SVHS video device; 15, power supplies and computer interface; 16, high precision linear positioning system; 17, last field lens.

perature is still very close to the supercooling before the crystal entered the growth vessel through the capillary. This corresponds to a vertical displacement in the morphology diagram of Brener *et al.* [8–10]. If the perturbation of the crystal is strong enough, the morphology will change from dendritic morphology to a high supercooling morphology—i.e., seaweed or doublon. Unfortunately the shifting down to colder regions leads out of the field of vision of our optical imaging system. To bring the crystal back into the field of vision we have to shift it up again. This shifting up does not reestablish the old stationary temperature distribution and

therefore we can observe a high supercooling morphology, long enough to quantitatively investigate it. After 180–240 s (corresponding to the time to grow the distance of about two to three side branch spacings) the system relaxes back to the stationary state—i.e., dendritic solidification.

There are two morphological transitions: the transition from dendritic growth to high supercooling growth forms and the relaxation back to dendrites. Both transitions are related to thermal gradients at the interface of the growing dendrite. In the following discussion the surface of the crystal can be considered to be isothermal (i.e., the Gibbs-
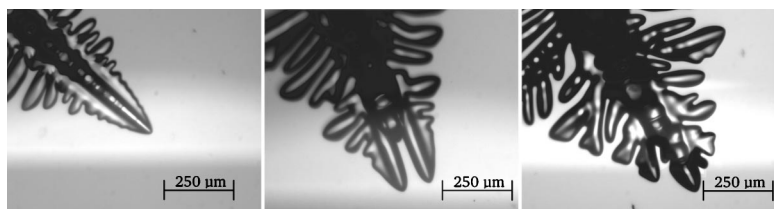

FIG. 2. Typical results of free three-dimensional thermal growth. (a) Dendritic morphology, (b) doublon morphology, and (c) seaweed morphology.

Thomson effect is small compared to the undercooling of the melt close to the solid-liquid interface). During the steady state of dendritic growth there are high thermal gradients in the melt close to the dendrite tip and these gradients at the crystal surface decrease along the fins with the distance to the tip. The growth velocities normal to the crystal interface are assumed to be proportional to the thermal gradient at the solid-liquid interface. A sudden shift of the crystal into the region of the growth vessel with a more or less homogeneous temperature distribution leads instantly to a homogeneous temperature distribution around the crystal with constant temperature gradients all over the crystal surface. Due to the increasing supercooling, the growth rate normal to the interface increases and is approximately the same at the tip and at the fins. This leads to an increase in the tip radius. An increase of the tip radius upon an increase of the supercooling is not compatible with steady-state growth. It leads away from the stability conditions of a steady-state dendrite and indeed tip splitting is observed. Now one has to consider, which structures are formed by this instability. The formation of side branches is one possibility but we observe doublon or seaweed growth. Flow due to the shift may increase the supercooling but the tip splitting is observed about 40–60 s after the shift when the flow due the shift has stopped.

After the formation of doublons two distinct and symmetric tips mutually stabilize their growth. No more tip splitting is observed [Fig. 2(b)]. The second possibility is the formation of seaweed morphology, which is characterized by successive tip splitting of any prominent tip (also side branches). This leads to a loss of symmetry of the crystal morphology, which is typical for seaweed [Fig. 2(c)]. The relaxation of doublons happens when the initially symmetrically growing fingers of the doublon are slightly perturbed. Then one of the fingers takes the lead and leaves the other behind. When the influence of the losing finger decreases, the winning finger relaxes back to dendritic growth. The relaxation from seaweed back to dendrites happens when the undercooling in the region of the crystal decreases and one of the prominent tips is stabilizing and not thickening again to a critical curvature that allows tip splitting.

IV. IMAGE PROCESSING AND TRANSFORMATIONS

In order to scientifically investigate the acquired images preliminary calculations are performed. The most vital step is to extract the contour line of the growing crystal. The images are first preprocessed by a gray level histogram stretching in order to obtain the maximal possible contrast enhancement. Consequently the images are filtered with the Marr-Hildreth-operator (Laplacian of Gaussian) [21] so that edges are enhanced. This filter transforms the problem of detecting the contour to finding transitions of zero crossings of the filtered data. As a next step an edge detecting routine is applied and the contour is extracted. Subsequently the contour must be cleaned of extraction artifacts and reordered. This step is not necessary for overall applied algorithms such as the shape detection method presented in the following. However, in order to calculate derivatives or angular distributions this reordering is needed. The last step of the contour

extraction process consists of scaling the contour according to its real size: the images taken show only a projection of the real shape; therefore, an appropriate scaling must be applied. A thorough introduction to the process of contour extraction in our images is given in [22].

The extracted contours of our experimental crystals can be classified by the human eye into three different classes: dendrites, doublons, and seaweed. Although this distinction is made very easily by a trained operator, it has some severe drawbacks: (i) it is only qualitative and (ii) a human operator must judge every image manually. In order to overcome these limitations we considered a computer-based approach to be desirable. The biggest obstacle to overcome therefore was to find a way to represent the given shapes of the crystal independently of the respective orientation, position, and size. It was thus necessary to find an invariant measure under rotation, scaling, and translation.

(i) The basic concept of this invariant representation is the well-known translation property of the Fourier transform (also known as Fourier shift theorem): Two functions $f_1(x,y)$ and $f_2(x,y)$ are given, which differ only by a displacement (x_0, y_0), so that

$$f_2(x,y) = f_1(x - x_0, y - y_0). \tag{1}$$

Their Fourier transforms F_1 and F_2 differ by a phase factor only:

$$F_2(k_x, k_y) = e^{-2\pi\iota(k_x x_0 + k_y y_0)} F_1(k_x, k_y), \tag{2}$$

where k_x, k_y are the spatial frequencies. It is thus clear that the intensities of the Fourier components are identical for both functions: $|F_i|^2 = F_i \overline{F_i}$ for $i = 1,2$ and therefore $|F_1| = |F_2|$. Hence, a shift in the spatial domain affects only the phase components of the functions in the frequency domain.

(ii) Rotation of the function $f(x,y)$ in the spatial domain by an angle θ causes the Fourier transform to be rotated by the same angle: $f(x \cos \theta + y \sin \theta, -x \sin \theta + y \cos \theta)$ becomes in the frequency domain

$$F(k_x \cos \theta + k_y \sin \theta, -k_x \sin \theta + k_y \cos \theta). \tag{3}$$

(iii) Scaling of the spatial axes with the scaling factor c causes an inverse scaling of the frequency axes: $f(cx, cy)$ becomes in the frequency domain

$$\frac{1}{c} F\left(\frac{k_x}{c}, \frac{k_y}{c}\right). \tag{4}$$

It is easy to see that only translational invariance is achieved in a straightforward way. However, it is possible to convert the functions into another coordinate system where scaling and rotation are represented as shifts. Let us consider the coordinate transformation of the log-polar mapping: Every point in a given domain [i.e., $(x,y)^T \in \mathbb{R}^2$] is transformed according to

$$x = e^\mu \cos \theta,$$

$$y = e^\mu \sin \theta, \tag{5}$$

where $r = \sqrt{x^2 + y^2} = e^\mu$, $\mu \in \mathbb{R}$ is the Euclidian distance to the origin, and $0 \le \theta \le 2\pi$ is the angle to the x axis. It is obvious

that this mapping is bijective. In this coordinate system scaling and rotation appear as shifts in the respective coordinates: scaling is related to

$$(cx, cy) \Rightarrow (\mu + \log c, \theta), \tag{6}$$

whereas rotation corresponds to

$$(x \cos(\theta + \phi) + y \sin(\theta + \phi), - x \sin(\theta + \phi) + y \cos(\theta$$
$$+ \phi)) \Rightarrow (\mu, \theta + \phi). \tag{7}$$

Taking the Fourier transform of a log-polar mapped function is therefore (by the properties of the Fourier transform) invariant under scaling and rotation. This invariance can also be achieved by the Fourier-Mellin-transform

$$F_M(k_x, k_y) = \int_{-\infty}^{\infty} \int_0^{2\pi} f(e^\mu \cos \theta, e^\mu \sin \theta) e^{\iota(k_x \mu + k_y \theta)} \mathrm{d}\mu \mathrm{d}\theta. \tag{8}$$

It can be shown that the Fourier-Mellin transform is identical to the combined log-polar and Fourier transform [23].

We assume two invariant operators F and F_M. Here F extracts the modulus of the Fourier transform and F_M the modulus of the Fourier-Mellin transform. When applying the combined operators to an image $f(x, y)$ we find

$$I_1 = [F_M \circ F] f(x, y). \tag{9}$$

The sign $\circ$ denotes the composition of different transformations applied to the image. The same operator can be applied to an image, which was translated, rotated, and scaled:

$$I_2 = [F_M \circ F \circ R(\theta) \circ S(s) \circ T(x_0, y_0)] f(x, y) \tag{10}$$

$$= [F_M \circ R(\theta) \circ F \circ S(s) \circ T(x_0, y_0)] f(x, y) \tag{11}$$

$$= \left[F_M \circ R(\theta) \circ S\left(\frac{1}{s}\right) \circ F \circ T(x_0, y_0) \right] f(x, y) \tag{12}$$

$$= [F_M \circ F] f(x, y) \tag{13}$$

Therefore the representation is indeed invariant under rotation, scaling, and translation. Hence the steps to achieve an RST invariant representation of an image consists of (i) a Fourier transform of the original image to remove translational differences, (ii) mapping of the calculated intensities into the (μ, θ) coordinate system (log-polar mapping) (i.e., rotational and scaling differences are transformed to shifts), and (iii) application of another Fourier transform in order to remove the newly transformed shifts. The RST invariant representation corresponds to the intensities of the transformed image.

This method of RST invariant representations is also used in the field of machine vision and the watermarking of images. The idea there is to add a nonvisible "water mark" in the phase components of the RST invariant representation and transform it back. The hope is that the watermark persists even if a digital image is transformed, cropped, printed, and scanned again. Further details can be found in [24–26].

The RST invariant representation leads to a unique characterization of the different morphologies. We have adopted
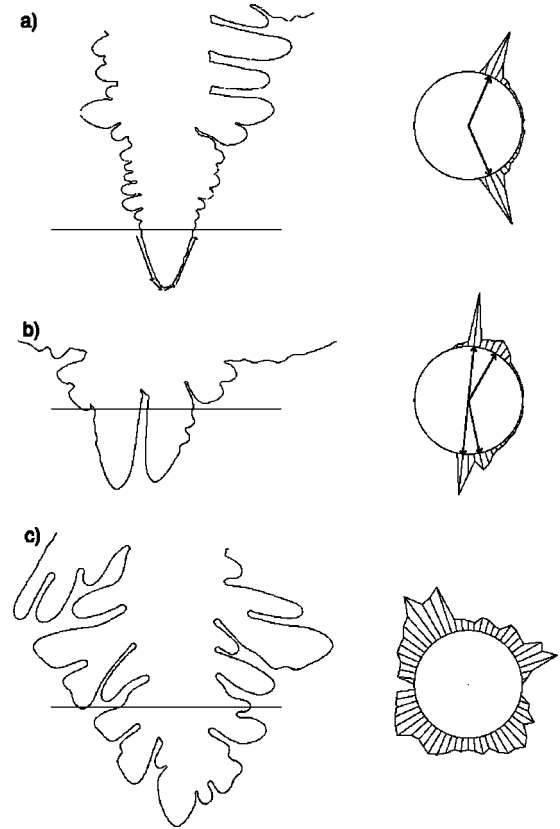

FIG. 3. Angular histograms of different morphologies are used to select typical examples for each morphology class for the extraction of prototypes. Each morphology shows a different amount of extrema in the region up to a chosen distance of 15-tip radii from the tip. (a) The dendritic morphology shows two distinct peaks, (b) the doublon morphology shows four peaks, and (c) the seaweed morphology shows a large number of uncorrelated peaks.

following strategy: For every morphology class we have selected a number of typical examples. For each manually selected example the contour was extracted and reordered [22]. We then have measured the angles from each contour point to the next and collected these angles into a histogram (angular histogram). The histogram is bent to a circle to provide an immediate correlation of the angular orientations to the complexity of the crystal shape. The histograms are shown in Fig. 3. We have determined the angular histogram of the contour line up to a chosen height of 15-tip radii from the tip and found that it is possible to *qualitatively* characterize the contours into the different morphology classes by counting the number of extrema occurring in the histogram. For a dendrite two extrema are found [Fig. 3(a)]. The length of the arrows next to the dendrite tip indicate approximately the peaks of the angular histogram. For the doublon morphology four extrema are found [Fig. 3(b)]. As for the seaweed morphology the distribution is very noisy and many different and uncorrelated extrema are found due to the strongly meandering shape of seaweed [Fig. 3(c)]. The distance of 15-tip radii was chosen because for higher values the influence of the side branches disturb the angular histogram and no meaningful selection can be made any more. For the seaweed and doublon morphology naturally no tip radius is defined. How-

ever, we have used the tip radius corresponding to the nominal supercooling of the melt before the experiment started as the corresponding length scale. The tip radius can be expressed as a function of the supercooling [17]:

$$R_{expt}(\Delta T) = (5.2 \pm 0.4)\Delta T^{-0.83 \pm 0.03}, \qquad (15)$$

where R_{expt} is given in μm and ΔT in K.

With the method of angular histograms it was possible to exclude much of the arbitrariness, which was naturally given by the manual selection of "beautiful" nondegenerated examples of each morphology class. Altogether we have used 44 contours of dendrites [selected from experiments of 6 different supercoolings between 80 and 180 mK, 17 contours of doublons (three different supercoolings between 80 and 130 mK), and 29 contours of seaweeds (three different supercoolings between 100 and 140 mK)] as a database. Although we use the capillary for seed selection, we observe that not all crystals grow along the same crystal orientation through the capillary; thus, the contours from different experiments do not grow along the same directions and have different positions.

The contours were subsequently transformed to the RST invariant representation. For every class all transformed example representants were averaged in order to extract a prototype for the respective class. We thus have found three 2D matrices of averaged intensities of a morphology class that are now considered to be prototypes:

$$I_{p_k}(i,j) = \frac{1}{n_k}\sum_{l=1}^{n_k} I_{k,l}(i,j), \quad 1 \leq i \leq N_x, \ 1 \leq j \leq N_y,$$
$$(16)$$

where k denotes the morphology index ($k=1$ dendritic, $k=2$ doublon, $k=3$ seaweed). N_x and N_y are the size of the 2D domain, and n_k is the number of the representants of the morphology class k. Here $I_{p_k}(i,j)$ and $I_{k,l}(i,j)$ are the intensities of the prototypes and the transformed representants, respectively.

In order to position a contour between the different classes we have used the following scheme: a given contour is first transformed to the RST invariant representation. Subsequently the Euclidean distance to the three prototypes is determined:

$$d_k = \sqrt{\sum_{j=1}^{N_y}\sum_{i=1}^{N_x}[I_C(i,j) - I_{p_k}(i,j)]^2}, \quad k = 1,2,3, \quad (17)$$

where d_k is the distance to the respective morphology class and $I_C(i,j)$ is the intensity of the transformed contour. The position of the contour in the morphology space is determined as follows: The morphology M of a contour C is given by the minimal distance to the prototypes:

$$M(C) = k_{\min d_k(C)},$$

where $M \in \{1,2,3\}$ determines the origin from which the other two distances are plotted: we have these three origins chosen to be $p_i = (\cos(\varphi_i), \sin(\varphi_i))^T$, $i=1,2,3$, with φ_i

$= \pi/6, \pi - \pi/6, 3\pi/2$. The position of the transformed contour is then given by

$$p_{M(C)} + r_a(p_a - p_{M(C)}) + r_b(p_b - p_{M(C)}), \qquad (18)$$

where a,b are the indices $\{k=1,2,3 \,|\, k \neq M(C)\}$. The values are determined by considering the following relations:

$$e_k = \frac{1}{c}[d_k - \min(d_k)] \qquad (19)$$

and

$$r_{a/b} = 1 - \frac{\arctan(e_k) + \pi/2}{\pi}. \qquad (20)$$

The function arctan was chosen to map all possible distances to 0.5–1 ($e_k \geq 0$, obviously $e_{M(C)}$ is 0). Therefore the values for $r_{a/b}$ are in the range $0 \leq r_{a/b} \leq 0.5$. Here 0.5 is the maximal distance that can occur. Otherwise the distance to at least one other morphology would become smaller and the detection would find a change in the morphology resulting in a different origin. This nontrivial mapping was chosen in order to improve the separation of the representants of the respective morphology classes.

We would like to note some points about implementational aspects of the presented method: The Fourier transform was implemented by using fast Fourier transform (FFT). It is well known that the FFT can only transform vectors of length that are equal to a power of 2 (2^n). We therefore have chosen a fixed size 512 ($n=9$) and have determined the bounding box of our contour. If the box was bigger than the chosen size, we have scaled the box accordingly to fit into the given size. Otherwise the contour was left as it was. As the RST transform is invariant under scaling we were allowed to pretransform the data without changing the results.

For the log-polar mapping we have adopted a bilinear back-transform scheme: instead of transforming the FFT intensities $I(x,y)$ to $I(\mu,\theta)$ we have calculated for the discrete values of (μ,θ) (arbitrarily chosen size 512 each) the resulting intensity by bilinear interpolation from the intensities of the FFT. Of course the size for the log-polar domain was chosen again accordingly so that it was possible to apply the 2D FFT.

V. RESULTS AND DISCUSSIONS

In Fig. 4 the temporal evolution of a growing xenon crystal is shown by a superposition of extracted contours. The time difference between two successive contours is $\Delta t = 5$ s. The first contour marked by arrow 1 can clearly be correlated to a dendritic morphology. With the temporal evolution the dendrite tip is successively becoming massive and the tip radius is increasing. As a consequence the tip velocity is remarkably slowing down as can be seen already qualitatively by looking at the distance between successive tip positions in the region depicted by arrow 2. When a critical curvature at the tip is reached the tip becomes unstable and performs a tip splitting leading to doublonic morphology.
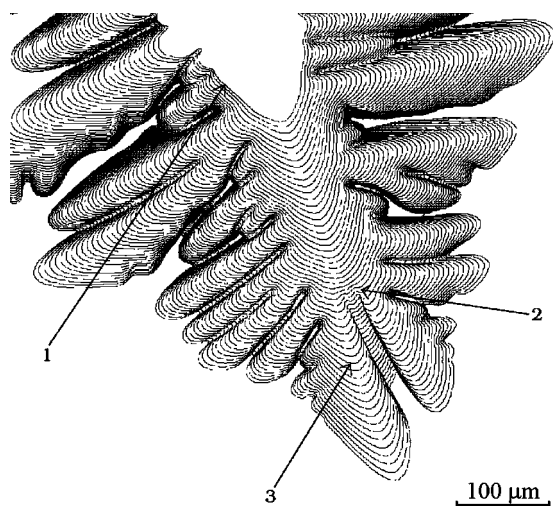
FIG. 4. Superimposed contours illustrate the temporal evolution of a crystal. The time interval between two successive contours is $\Delta t = 5$ s. A morphology change from dendritic (arrow 1) to doublonic (arrow 3) morphology can be observed. The transition takes place by an increase of the tip radius, which leads to a tip splitting (arrow 2).

Due to the method, morphology changes are induced we are only able to observe transient morphology states as mentioned in Sec. III. After a while (as a consequence of the fact that the experimental conditions at the two tips are not identical) one of the tips will eventually have an advantage over the other and outgrow it. The winning tip will after a relaxation time, when the influence of the decelerating finger of the doublon is more and more fading away, relax to a dendritic morphology again. This is depicted in Fig. 5. We have applied the RST invariant prototype matching to this morphology change. The result is given in Fig. 6. The example representants, which were used to extract the prototypes, are plotted as circles in their respective morphology class. It can be seen that the first contours are found to be dendritic as expected. Simultaneously with the increase of the tip radius
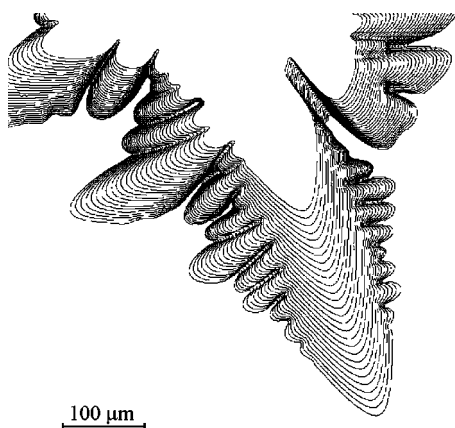

FIG. 5. Superimposed contours of the relaxation of the doublon morphology to dendritic morphology. Due to experimental inhomogeneities, the left tip has a small advantage over the right one and outgrows it and thus evolves back to a single tip dendritic morphology.
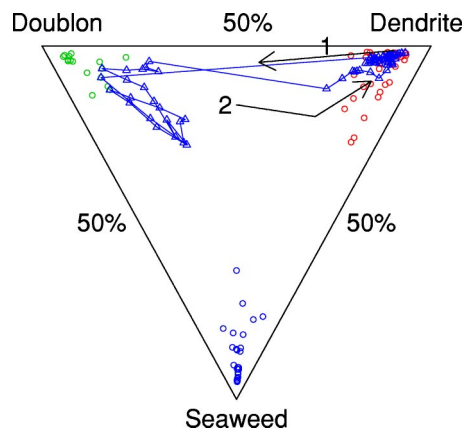

FIG. 6. RST invariant morphology detection: the transition from dendritic to doublonic morphology and the relaxation back to a dendrite is marked as a path (triangles) in the morphology space. The arrows 1 and 2 indicate the directions of the transitions. The circles in each corner represent the position of the examples chosen to extract the prototypes.

before the tip splitting the distance to the dendrite prototype is increasing. Shortly after the splitting the morphology detection indicates a morphology change. Although the detected class of the contours is found to be doublonic, the contours remain initially quite far from the doublon prototype. With the increasing size of the tips growing in parallel, however, it moves closer to the prototype. Due to the transient nature of this morphology change the influence of the outgrowing winning tip becomes noticeable, which leads to an increased distance from the doublonic prototype again. As the winning tip "feels" less influence from the other tip the morphological position moves rather abruptly back to the dendritic morphology as depicted by arrow 2 in Fig. 6.

An even more complex behavior of morphological transitions is given in Fig. 7. Again the evolution of the crystal is shown by superimposed contours with time steps $\Delta t = 5$ s. It is easy to see by eye that the starting morphology is dendritic. The same scenario as in the first example occurs in the beginning: the increase of the tip radius corresponds also to an increase of the distance (arrow 1) from the dendritic prototype. Again a tip splitting leads to a change of the morphology class to a doublon (arrow 2). However, this time the doublonic structure is not able to evolve as the right tip is taking the lead immediately and grows bigger increasing the tip radius and a little bit later the left tip starts behaving as a degenerate side branch very near the (winning) tip. The structure altogether evolves into a seaweed morphology. It can easily be seen that in the presented morphology plot (Fig. 8) a smooth transition between the three morphology classes is found.

For the first time it is possible to quantitatively specify paths of morphology transitions in the morphology space and to compactify results of experimentally grown diffusional growth structures into easily readable summaries of different transitions.

We have presented a method of RST invariant morphology detection based on properties of the Fourier transform and the log-polar mapping. We have shown that it is possible
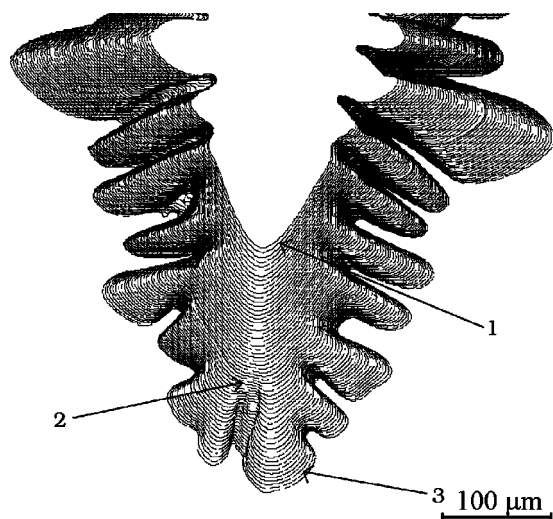
FIG. 7. Superimposed contours of a three morphology transition: the starting morphology is dendritic (arrow 1). After a tip splitting (arrow 2) it remains for a short while a doublon; however, one tip immediately takes advantage and the morphology changes to seaweed (arrow 3).
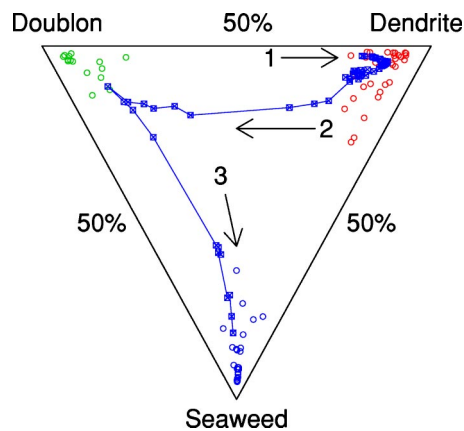

FIG. 8. RST invariant morphology detection: the transition from dendritic to a short period of doublon and the change to the seaweed morphology is marked as a smooth and continuous path (squares) in the morphology space. The arrows 1–3 indicate the directions of the transitions. The circles in each corner represent the position of the examples chosen to extract the prototypes.

to quantitatively describe the morphology transitions as paths in the morphology space. It was stated that the changes of patterns are usually smooth, however with the notion that the distances between two successive images tend to get bigger upon a qualitative change of the respective morphology class.

We would like to mention that this method might have also a small drawback: when analyzing bigger structures with side branches of the size comparable to the tip or even bigger, it might happen that the detection may fail. For example, a seaweed structure could be interpreted as a dendrite because of a prominent side branch. The same could happen with a dendrite having two big neighboring side branches. Due to the rotational invariance, the detection would eventually pretend to find a doublon. We would like to emphasize that this is not a failure of the method itself but rather a logical consequence of analyzing rotational invariant structures. We have found, however, that this case happened only on two of 650 analyzed contours, which proves that the pre-

sented method is rather robust on detection. With this method it is possible to overcome the limitations of a human operator: namely, we can automate the process and receive quantitative information about morphologies and their development with time. It should be noted that this quantitative measure should not be interpreted as, for example, "how dendritic" a structure is. It is rather possible to (i) qualitatively classify a given structure instead and (ii) furthermore retrieve quantitative information about which additional features (i.e., doublonic, seaweed like, dendritic) the given structures possess depending on the distance from the respective morphology prototype.

We believe that the presented method could be of some use for other fields of research where qualitative and quantitative information of different classes of patterns has to be found and detected.

[1] S. S. Augustithis, *Atlas of the Textural Patterns of Ore Minerals and Metallogenetic Processes* (de Gruyter, Berlin, 1995).

[2] J. S. Langer, in *Chance and Matter*, Les Houches, Sessions XLVI, 1986, edited by J. Souletie, J. Vannimenus, and R. Stora (Elsevier Science, Amsterdam, 1987), pp. 629–711.

[3] J. P. Gollub and J. S. Langer, Rev. Mod. Phys. **71**, S396 (1999).

[4] *Branching in Nature*, edited by V. Fleury, J. F. Gouyet, and M. Leonetti (Springer, Berlin, 2001).

[5] *Solids Far From Equilibrium*, edited by C. Godrèche (Cambridge University Press, Cambridge, England, 1992).

[6] D. M. Stefanenscu, *Science and Engineering of Casting Solidi-fication* (Kluwer Academic, New York, 2002).

[7] L. I. Rubinstein, *The Stefan Problem* (American Mathematical Society, Providence, RI, 1971).

[8] E. Brener, K. Kassner, H. Müller-Krumbhaar, and D. Temkin, Int. J. Mod. Phys. C **3**, 825 (1992).

[9] E. Brener, H. Müller-Krumbhaar, and D. Temkin, Europhys. Lett. **17**, 535 (1992).

[10] E. Brener, H. Müller-Krumbhaar, and D. Temkin, Phys. Rev. E **54**, 2714 (1996).

[11] S. Akamatsu, G. Faivre, and T. Ihle, Phys. Rev. E **51**, 4751 (1995).

[12] I. Stalder and J. H. Bilgram, Europhys. Lett. **56**, 829 (2001).

[13] H. M. Singer, Master thesis, Eidgenössische Technische Hochschule, Zürich-CH, 2001.

[14] M. E. Glicksman, R. J. Schaefer, and J. D. Ayers, Metall. Trans. A **7A**, 1747 (1976).

[15] A. C. Sinnock and B. L. Smith, Phys. Rev. **181**, 1297 (1969).

[16] *Rare Gas Solids*, edited by M. L. Klein and J. A. Venables (Academic, New York, 1977).

[17] E. Hürlimann, R. Trittibach, U. Bisang, and J. H. Bilgram, Phys. Rev. A **46**, 6579 (1992).

[18] U. Bisang and J. H. Bilgram, Phys. Rev. E **54**, 5309 (1996).

[19] E. Brener and D. Temkin, Phys. Rev. E **51**, 351 (1995).

[20] A. Karma, Y. H. Lee, and M. Plapp, Phys. Rev. E **61**, 3996 (2000).

[21] D. Marr and E. Hildreth, Proc. R. Soc. London, Ser. B **207**, 187 (1980).

[22] H. M. Singer and J. H. Bilgram, J. Cryst. Growth **261**, 122 (2004).

[23] R. D. Brandt and F. Lin, Pattern Recogn. Lett. **17**, 1001 (1996).

[24] J. J. K. Ruanaidh and T. Pun, in *Proceedings of ICIP 1997*, IEEE International Conference on Image Processing, edited by IEEE Computer Society (IEEE, Los Alamitos, CA, 1997), p. 536.

[25] J. J. K. Ruanaidh and T. Pun, Signal Process. **66**, 303 (1998).

[26] B. S. Reddy and B. N. Chatterji, IEEE Trans. Image Process. **5**, 1266 (1996).